IEEE Access
Multidisciplinary | Rapid Review | Open Access Journal

Received November 3, 2020, accepted December 5, 2020, date of publication December 14, 2020,
date of current version December 31, 2020.

Digital Object Identifier 10.1109/ACCESS.2020.3044589

Aerodynamic Statistics-Based Trajectory Estimation of Hypersonic Maneuvering Target

YUNPENG CHENG[1], SHUO TANG[1,2], SHI LYU[1,2], MANQIAO WU[3], AND HAO QIAO[4]
[1]School of Astronautics, Northwestern Polytechnical University, Xi'an 710072, China
[2]Shaanxi Key Laboratory of Aerospace Flight Vehicle Technology, Xi'an 710072, China
[3]Science and Technology on Space Physics Laboratory, Beijing 100076, China
[4]Xi'an Institute of Modern Control Technology, Xi'an 710065, China

Corresponding author: Shi Lyu (yorklianpei@gmail.com)

ABSTRACT Trajectory tracking and estimation of hypersonic glide vehicles (HGVs) is a very challenging issue in the defense systems. Insufficient knowledge about the HGV and inaccurate dynamic models for the accelerating HGV are the main challenges in this regard. In the present study, an integrated nonlinear Markov acceleration model is established to formulate the nonlinear dynamic characteristics of HGVs. Since the aerodynamic accelerations of the HGV are dominant and the corresponding aerodynamic coefficients are unknown, a statistics-based aerodynamic model is proposed. The proposed aerodynamic model is capable of providing primary information of the aerodynamic characteristics even without knowing the configuration of the HGV. Then, considering the maneuver mode of the vehicle, the iterative extended Kalman filter (IEKF) is applied to track the trajectory of the HGV by using the proposed model. Obtained results from the numerical simulation for the equilibrium glide mode and skip maneuver mode indicate that the proposed model can effectively improve the velocity estimation accuracy by about 40%-50% and acceleration estimation accuracy by about 20%-50% in the given examples.

INDEX TERMS Hypersonic glide vehicle, target tracking, maneuvering model, state estimation.

I. INTRODUCTION

Studies show that flexible maneuvers can be carried out by hypersonic glide vehicles (HGVs) to increase their survival rate in real operations [1]. This capability originates from the high maneuverability of HGVs. As a result, the trajectory tracking and estimation of HGVs are more challenging for the defense systems, when the comparison is made with that of ballistic vehicles. Generally, trajectory tracking and estimation are fulfilled through a filter, which combines measured data received from the radar and that of the reference model [2]. Accordingly, the reference model has a significant impact on the estimation accuracy of the trajectory [3], [4]. This is especially more pronounced for state variables, which cannot be measured directly. For ballistic targets, the ballistic coefficient or accelerations are almost constant or slowly change so that these coefficients can be modelled as a constant or a first-order Markov process [5]. Consequently, the target state of the ballistic target, including the velocity, position and acceleration can be accurately estimated. However, maneuvers of the HGV rely on the aerodynamic forces within the atmosphere so that the drag and lift accelerations are prominent and may rapidly change [6]. Since the acceleration data of HGVs can be hardly detected directly by the radar of the defense system, establishing an appropriate reference model of the filter is essential to accurately estimate the instantaneous state of the HGV.

Almost all maneuvering target trajectory estimation methods are model-based. An excellent tracking model should describe the true process of target motion and the moving characteristics. Reviewing the literature indicates that filter models for trajectory tracking can be roughly divided into two categories, including the kinematic models and the dynamic models. In this regard, different kinematic models such as Singer model [7], second-order time-dependent model [8], constant turning model [9], semi-Markov model [10], jerk model [11] and adaptive current statistical model [12], have been proposed so far. Studies show that although these

The associate editor coordinating the review of this manuscript and approving it for publication was Yuan Zhuang.

models have reasonable real-time performance, they have some inherent drawbacks such as the lack of characterization of innate dynamics and inability to consider the nonlinearity of the dynamics. In order to develop new dynamic models, the concept of maneuvering coefficients was introduced to describe the motion of a maneuvering missile [13]. Then the state augmentation method was adopted to estimate the ballistic and maneuvering coefficients [14]. Fan *et al*. [15] introduced the angle of attack and the bank angle as two control variables in the Gaussian models and applied the cubature Kalman filter to estimate the target state with fixed control variables. In the foregoing studies, key parameters formulating the accelerations of the HGV are modelled as constants with zero acceleration derivatives or linear Gauss-Markov processes. However, the dynamic pressure, which has a great impact on the accelerations of the HGV, has not been fully considered yet. Moreover, many studies were performed to track tactical ballistic missiles adopting spiraling motion during the reentering phase. Dubois-Matra and Bishop [16] implemented time derivatives in a Kalman filter system and developed a flight model to track a spiraling maneuvering reentry vehicle accompanied by decoys. Tapiero and Bishop [17] established a model considering stochastic uncertainty parameters from ballistic geometry for tracking spiraling reentry vehicles. More recently, Hough [18] proposed nonlinear Markov acceleration models with variable process noise amplitudes. He established the dynamics of the accelerations and decomposed affecting factors into several components, which can describe the dynamics of HGVs. However, there are still some unsolved challenges to be faced. First, due to insufficient knowledge about the noncooperative HGV, configuration parameters and aerodynamic coefficients are unknown to the defense system. Consequently, the model mismatch, which can significantly deteriorate the tracking accuracy, may occur. Second, the accelerations of the HGV cannot be measured directly through the radar. Consequently, the nonlinear dynamics coupled with an inaccurate estimation of the accelerations may magnify tracking errors of the vehicle state.

Inspired by the aforementioned analysis, in the present study, it is intended to propose a statistics-based nonlinear dynamic model to solve the trajectory tracking problem of HGVs. To this end, the dynamic model of the acceleration components related to the position, velocity, atmospheric parameters and statistics of expected manoeuvres, is established. Since the configuration of the target HGV is unknown, a statistical analysis is initially performed for a family of HGVs to acquire the initial information of the primary aerodynamic characteristics of HGVs. Finally, the IEKF algorithm is conducted to accomplish the trajectory tracking.

II. DYNAMIC MODELS OF HGVs

In order to establish the dynamic models of the HGV, the earth is assumed as a homogeneous sphere. Considering the rotation of the earth, the three-dimensional point-mass dynamics of the HGV are constructed in a semi-speed coordinate frame (VTC) [19]. It should be indicated that the sideslip angle of the HGV is neglected in all calculations.

$$\begin{cases} \dfrac{dr}{dt} = v\sin\gamma \\ \dfrac{d\theta}{dt} = \dfrac{v\cos\gamma\sin\psi}{r\cos\phi} \\ \dfrac{d\phi}{dt} = \dfrac{v\cos\gamma\cos\psi}{r} \\ \dfrac{dV}{dt} = -a_D - g\sin\gamma \\ \dfrac{d\gamma}{dt} = \dfrac{1}{v}\left[a_L\cos\sigma + \left(\dfrac{v^2}{r} - g\right)\cos\gamma\right] + C_\gamma \\ \dfrac{d\psi}{dt} = \dfrac{1}{v}\left[\dfrac{a_L\sin\sigma}{\cos\gamma} + \dfrac{v^2}{r}\cos\gamma\sin\psi\tan\phi\right] + C_\psi \end{cases} \tag{1}$$

where r, θ, ϕ, v, γ, ψ are radial distance from the centre of the Earth to the vehicle, longitude, latitude, velocity of the HGV, flight path angle and the velocity heading angle, respectively. Moreover, σ and g are the bank angle and the gravity acceleration, respectively. C_γ and C_ψ are additional terms caused by the rotation of the earth [20].

The magnitudes of the drag and lift accelerations (a_D and a_L) are related to aerodynamic coefficients, reference area, mass and dynamic pressure [19]. These parameters can be mathematically expressed as the following:

$$\begin{cases} a_D = \dfrac{qC_DS}{m} \\ a_L = \dfrac{qC_LS}{m} \end{cases} \tag{2}$$

where S and m denote the reference area and mass of the vehicle, respectively. Furthermore, C_D and C_L are drag and lift coefficients of HGV, respectively. $q = \rho v^2/2$ is the dynamic pressure and ρ is the atmospheric density, which can be expressed as the exponential function of height, in the form below [19]:

$$\rho = \rho_0 e^{-h/hs} \tag{3}$$

where ρ_0 =1.225 kg/m^3 is the atmospheric density at the sea level and h denotes the altitude of the target distance from the sea level. Meanwhile, $h = r - R_e$, where R_e is the radius of the earth. Finally, $hs = 6700$ m is a constant.

III. GLIDING DYNAMICS FOR TRACKING

In order to track the trajectory of the HGV, the dynamic model is a base for the state estimation. In this section, the dynamic model of acceleration components for the HGV is derived.

A. DYNAMICS OF HGVs

Radar reference coordinate system (RRCS): In this coordinate system, the origin coincides with the radar station position, while unit vectors of X- and Y-axes are located in the tangent plane of the earth's reference sphere, along East and North directions, respectively. Meanwhile, the unit vector of the Z-axis is perpendicular to the local horizontal plane. Accordingly, the RRCS is also called the local East-North-Up (ENU) geographic coordinate system.

During the gliding phase, the HGV motion relative to the radar reference coordinate can be mathematically expressed as:

$$\begin{aligned}\frac{d\boldsymbol{r}}{dt} &= \boldsymbol{v}\\ \frac{d\boldsymbol{v}}{dt} &= \boldsymbol{g}+\boldsymbol{a}-\boldsymbol{\omega_e}\times(\boldsymbol{\omega_e}\times\boldsymbol{r})-2\boldsymbol{\omega_e}\times\frac{d\boldsymbol{r}}{dt}\end{aligned} \tag{4}$$

where $\boldsymbol{r}$ and $\boldsymbol{v}$ represent the center distance vector and the velocity vector of HGV, respectively. Moreover, $\boldsymbol{a}$ denotes the acceleration of HGV originating from aerodynamic forces; $\boldsymbol{\omega_e}$ is the angular velocity of the earth; $-\boldsymbol{\omega_e}\times(\boldsymbol{\omega_e}\times\boldsymbol{r})$ denotes centrifugal acceleration; $-2\boldsymbol{\omega}_e\times\dot{\boldsymbol{r}}$ denotes Coriolis acceleration; The gravity acceleration of gravity can be expressed as:

$$\boldsymbol{g}(\boldsymbol{r}) = -\frac{\mu}{r^2}\left(\frac{\boldsymbol{r}}{r}\right) \tag{5}$$

where μ is the gravitational parameter of the earth.

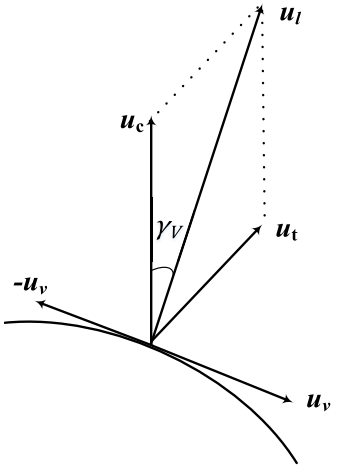

FIGURE 1. Decomposition of the aerodynamic acceleration vector.

Fig. 1 presents the decomposition of the aerodynamic acceleration vector in VTC [21]. Where $\boldsymbol{u}_v$, $\boldsymbol{u}_\mathrm{t}$ and $\boldsymbol{u}_\mathrm{c}$ are unit vectors of each axis in the VTC coordinate. Furthermore, $\boldsymbol{a}_\mathrm{d}$, $\boldsymbol{a}_\mathrm{t}$ and $\boldsymbol{a}_\mathrm{c}$ are acceleration components of the drag, turn and climb, respectively. These components can be expressed as follows:

$$\begin{aligned}\boldsymbol{a}_\mathrm{d} &= -a_\mathrm{d}\left(\boldsymbol{u}_v/u_v\right), \boldsymbol{u}_v = \boldsymbol{v}-\boldsymbol{\omega}_e\times r\\ \boldsymbol{a}_\mathrm{t} &= a_\mathrm{t}\left(\boldsymbol{u}_\mathrm{t}/u_\mathrm{t}\right), \boldsymbol{u}_\mathrm{t} = \boldsymbol{r}\times\boldsymbol{u}_v\\ \boldsymbol{a}_\mathrm{c} &= a_\mathrm{c}\left(\boldsymbol{u}_\mathrm{c}/u_\mathrm{c}\right), \boldsymbol{u}_\mathrm{c} = \boldsymbol{u}_v\times\boldsymbol{u}_\mathrm{t}\end{aligned} \tag{6}$$

or,

$$\begin{aligned}\boldsymbol{a} &= \boldsymbol{a}_\mathrm{d}+\boldsymbol{a}_\mathrm{t}+\boldsymbol{a}_\mathrm{c}\\ &= a_D\boldsymbol{u_v}+a_L\sin\gamma_V\boldsymbol{u}_\mathrm{t}+a_L\cos\gamma_V\boldsymbol{u}_\mathrm{c}\end{aligned} \tag{7}$$

where γ_V is the bank angle. The aerodynamic acceleration vector can be decomposed in the VTC coordinate system [22]. This can be mathematically expressed as the following:

$$a_\mathrm{d} = \kappa_\mathrm{d}q, a_\mathrm{t} = \kappa_\mathrm{t}q, a_\mathrm{c} = \kappa_\mathrm{c}q$$

$$\begin{aligned}\kappa_\mathrm{d} &= C_DS/m\\ \kappa_\mathrm{t} &= C_LS\sin\gamma_V/m\\ \kappa_\mathrm{c} &= C_LS\cos\gamma_V/m\end{aligned} \tag{8}$$

where κ_d, κ_t and κ_c denote the drag, lateral and longitudinal aerodynamic parameters, respectively. The total lift acceleration and aerodynamic parameters are defined as $a_L = \sqrt{a_\mathrm{t}^2+a_\mathrm{c}^2}$ and $\kappa_L = \sqrt{\kappa_\mathrm{t}^2+\kappa_\mathrm{c}^2}$, respectively. Corresponding to the components of the lift acceleration, the angle of attack is also decomposed into the lateral and longitudinal components.

Lift coefficient $C_L(\alpha,Ma)$ is a function of the angle of attack and Mach number, where the Mach number can be calculated from the following expression:

$$Ma\left(v,h\right) = v/c_s\left(h\right) \tag{9}$$

It is worth noting that the sound velocity cs is a highly nonlinear function [19]. Drag coefficient can be described in the form of the drag pole curve [23]:

$$C_D = C_D^0+KC_L^2 \tag{10}$$

where C_D^0 is the zero-lift drag coefficient when no lift is generated by the HGV and K is a constant.

$$C_D^0 = \frac{C_L^*}{2\left(\frac{C_L}{C_D}\right)_{\max}}, K = \frac{C_D^0}{C_L^{*2}} \tag{11}$$

The critical lift coefficient C_L^* is the lift coefficient with a maximum lift-to-drag ratio.

B. ACCELERATION MODEL BASED ON NONLINEAR MARKOV PROCESSES

Maneuver accelerations of HGVs are affected by a few trajectory parameters and guidance commands, including the height, velocity, atmospheric parameters, aerodynamic characteristics of the HGV, angle of attack and the bank angle. Dubois-Matra [16] and Tapiero [17] investigated the time derivative of acceleration components to have a deep insight into the dynamics of acceleration.

1) COMPONENTS OF THE LIFT ACCELERATION MODEL

In order to simplify the calculations without loss of generality, parameters a_t and a_c are replaced with a_j (a_j{j=t, c}). Based on Eq. (8), the derivative of a_j can be expressed in the form below:

$$\dot{a}_\mathrm{j} = \left(\frac{\partial\kappa_\mathrm{j}}{\partial\alpha_\mathrm{j}}\dot{\alpha}_\mathrm{j}+\frac{\partial\kappa_\mathrm{j}}{\partial Ma}\dot{M}a\right)q+\kappa_\mathrm{j}\dot{q} \tag{12}$$

Assuming that lateral and longitudinal components of the angle of attack are independent of each other, the first-order Markov processes can be established as:

$$\dot{\alpha}_\mathrm{j} = \frac{1}{\tau_\mathrm{j}}\left(\alpha_{\mathrm{j,ctrl}}-\alpha_\mathrm{j}\right) \tag{13}$$

where τ_j is the time constant and $\alpha_{\mathrm{j,ctrl}}$ is a term that controls the angle of attack.

Based on Eqs. (3), (8), (9) and (13), each term in the right hand side of Eq. (12) can be rewritten as the following:

$$q\frac{\partial \kappa_{\mathrm{j}}}{\partial \alpha_{\mathrm{j}}}\dot{\alpha}_{\mathrm{j}} = q\frac{\partial \kappa_{\mathrm{j}}}{\partial \alpha_{\mathrm{j}}}\frac{1}{\tau_{\mathrm{j}}}\left(\alpha_{\mathrm{j,ctrl}} - \alpha_{\mathrm{j}}\right) = \frac{1}{\tau_{\mathrm{j}}}\left(a_{\mathrm{j,ctrl}} - a_{\mathrm{j}}\right) \tag{14}$$

$$q\frac{\partial \kappa_{\mathrm{j}}}{\partial Ma}\dot{Ma} = q\frac{\partial \kappa_{\mathrm{j}}}{\partial Ma}\frac{\partial Ma}{\partial v}\dot{v} = \frac{\partial \kappa_{\mathrm{j}}}{\partial Ma}\frac{1}{c_s}\dot{v}q \tag{15}$$

$$\kappa_{\mathrm{j}}\dot{q} = \kappa_{\mathrm{j}}\left(\frac{\partial q}{\partial h} + \frac{\partial q}{\partial v}\right) = \kappa_{\mathrm{j}}\left(-\frac{q}{hs}\dot{h} + \frac{2q}{v}\dot{v}\right) \tag{16}$$

where $a_{\mathrm{j,ctrl}}$ is the acceleration guidance command. The velocity derivative can be calculated in the form below:

$$\dot{v} = \frac{\boldsymbol{v}^{\mathrm{T}}\boldsymbol{g}}{v} - a_{\mathrm{d}} \tag{17}$$

Meanwhile, the derivative of the flight height can be calculated from the following expression:

$$\dot{h} = \frac{\boldsymbol{v}^{\mathrm{T}}\boldsymbol{r}}{r} \tag{18}$$

The lift acceleration models yield the following result:

$$\begin{aligned}\dot{a}_{\mathrm{j}} &= \frac{1}{\tau_{\mathrm{j}}}\left(a_{\mathrm{j,ctrl}} - a_{\mathrm{j}}\right) + \frac{\partial \kappa_{\mathrm{j}}}{\partial Ma}\frac{1}{c_s}\dot{v}q + \kappa_{\mathrm{j}}\left(-\frac{q}{hs}\dot{h} + \frac{2q}{v}\dot{v}\right)\\ &= \frac{1}{\tau_{\mathrm{j}}}\left(a_{\mathrm{j,ctrl}} - a_{\mathrm{j}}\right) + \left(\frac{\partial \kappa_{\mathrm{j}}}{\partial Ma}\frac{1}{c_s}q + \frac{2\kappa_{\mathrm{j}}q}{v}\right)\left(\frac{\boldsymbol{v}^{\mathrm{T}}\boldsymbol{g}}{v} - a_{\mathrm{d}}\right)\\ &\quad - \frac{\kappa_{\mathrm{j}}q}{hs}\frac{\boldsymbol{v}^{\mathrm{T}}\boldsymbol{r}}{r} = \left(\underbrace{\left(\frac{\boldsymbol{v}^{\mathrm{T}}\boldsymbol{g}}{v} - a_{\mathrm{d}}\right)\frac{2}{v} - \frac{1}{hs}\frac{\boldsymbol{v}^{\mathrm{T}}\boldsymbol{r}}{r}}_{S_1} - \underbrace{\frac{1}{\tau_{\mathrm{j}}}}_{S_2}\right)a_{\mathrm{j}}\\ &\quad + \underbrace{\frac{\partial \kappa_{\mathrm{j}}}{\partial Ma}\frac{1}{c_s}q\left(\frac{\boldsymbol{v}^{\mathrm{T}}\boldsymbol{g}}{v} - a_{\mathrm{d}}\right)}_{S_3} + \underbrace{\frac{1}{\tau_{\mathrm{j}}}a_{\mathrm{j,ctrl}}}_{S_4}\end{aligned} \tag{19}$$

Eq. (19) shows that the lateral and longitudinal lift accelerations a_{t} and a_{c} are established by nonlinear first-order Markov processes. The term S_1 is determined by the vehicle's state and leads to the nonlinearity in the dynamic model of the lift accelerations. If $S_1 = 0$, the dynamic model of the lift accelerations follows the linear Markov process. Moreover, the terms S_2 and S_3 denote the maneuvering frequency corresponding to aerodynamic parameters and the bias of the lift acceleration induced by the change of the state variables, respectively. It should be indicated that in the term S_3 the aerodynamic coefficients should be known. Furthermore, the term S_4 stands for the variation of the lift acceleration caused by guidance commands. Considering that the guidance commands of the acceleration $a_{\mathrm{j,ctrl}}$ are generally not obtained by the defense industry, it can be assumed as $a_{\mathrm{j,ctrl}} = 0$ [18]. The terms S_3 and S_4 change the mean value of the distribution of the lift acceleration.

In the acceleration components caused by the lifting force, only the time constant τ_{j} and the partial derivative of aerodynamic parameters to Mach number $\frac{\partial \kappa_{\mathrm{j}}}{\partial Ma}$ are not directly correlated to the state variables of the HGV. It should be indicated that the time constant can be set empirically. The partial derivative of aerodynamic parameters to Mach number is described in section IV.

2) DRAG ACCELERATION MODEL

According to the description of the drag pole curve in Eqs. (8)-(10), the total differential of the drag acceleration is mathematically expressed as:

$$\dot{a}_{\mathrm{d}} = \left(\frac{\partial \kappa_{\mathrm{d}}}{\partial v}\dot{v} + \frac{\partial \kappa_{\mathrm{d}}}{\partial C_L}\dot{C}_L\right)q + \kappa_{\mathrm{d}}\dot{q} \tag{20}$$

Moreover,

$$q\frac{\partial \kappa_{\mathrm{d}}}{\partial v}\dot{v} = q\frac{\partial \kappa_{\mathrm{d}}}{\partial Ma}\frac{\partial Ma}{\partial v}\dot{v} = \frac{\partial \kappa_{\mathrm{d}}}{\partial Ma}\frac{\dot{v}q}{c_s} \tag{21}$$

$$\begin{aligned}q\frac{\partial \kappa_{\mathrm{d}}}{\partial C_L}\dot{C}_L &= q\frac{\partial C_D}{\partial C_L}\dot{\kappa}_L \cong q\frac{1}{n}\left(\frac{\partial \kappa_L}{\partial \alpha}\dot{\alpha} + \frac{\partial \kappa_L}{\partial Ma}\dot{Ma}\right)\\ &\cong \frac{1}{n}\frac{1}{\tau_L}\left(a_{Lc} - a_L\right) + q\frac{1}{n}\frac{\partial \kappa_L}{\partial Ma}\frac{1}{c_s}\dot{v}\end{aligned} \tag{22}$$

where n is the lift-drag ratio of the HGVs, which can be obtained by distribution statistics. Then:

$$\kappa_{\mathrm{d}}\dot{q} = \kappa_{\mathrm{d}}\left(\frac{\partial q}{\partial h} + \frac{\partial q}{\partial v}\right) = \kappa_{\mathrm{d}}\left(-\frac{q}{hs}\dot{h} + \frac{2q}{v}\dot{v}\right) \tag{23}$$

The drag acceleration model for the estimation is described as:

$$\begin{aligned}\dot{a}_{\mathrm{d}} &= \underbrace{\left(\frac{2}{v}\frac{\boldsymbol{v}^{\mathrm{T}}\boldsymbol{g}}{v} - \frac{\partial \kappa_{\mathrm{d}}}{\partial Ma}\frac{1}{c_s}q - \frac{1}{n}\frac{\partial \kappa_L}{\partial Ma}\frac{1}{c_s}q - \frac{1}{hs}\frac{\boldsymbol{v}^{\mathrm{T}}\boldsymbol{r}}{r}\right)a_{\mathrm{d}} - \frac{2}{v}a_{\mathrm{d}}^2}_{Q_1}\\ &\quad \underbrace{- \frac{1}{n}\frac{1}{\tau_L}a_L}_{Q_2} + \underbrace{\frac{\partial \kappa_{\mathrm{d}}}{\partial Ma}\frac{1}{c_s}\frac{\boldsymbol{v}^{\mathrm{T}}\boldsymbol{g}}{v}q + \frac{1}{n}\frac{\partial \kappa_L}{\partial Ma}\frac{1}{c_s}\frac{\boldsymbol{v}^{\mathrm{T}}\boldsymbol{g}}{v}q}_{Q_3} + \underbrace{\frac{1}{n}\frac{1}{\tau_L}a_{Lc}}_{Q_4}\end{aligned} \tag{24}$$

where, the autopilot time constant is $\tau_L = (\tau_{\mathrm{t}} + \tau_{\mathrm{c}})/2$, and the total lift acceleration guidance command is $a_{Lc} = \sqrt{a_{\mathrm{t,}ctrl}^2 + a_{\mathrm{c,}ctrl}^2}$.

Eq. (24) shows that the drag acceleration is determined by the nonlinear and inhomogeneous differential equation, which includes the linear and quadratic terms of the drag acceleration (Term Q_1), the total lift acceleration (Term Q_2), variable coefficient depending on the altitude, velocity and partial derivatives of aerodynamic parameters to Mach number (Term Q_3) and the guidance command of the total lift acceleration (Term Q_4). In the drag acceleration component, the partial derivative of aerodynamic parameters to Mach number $\frac{\partial \kappa_{\mathrm{d}}}{\partial Ma}$, $\frac{\partial \kappa_L}{\partial Ma}$ and the lift drag ratio n of the HGVcan be obtained by statistical methods, which is described in section IV.

IV. AERODYNAMIC CHARACTERISTICS STATISTICS

In Eqs. (19) and (24), the partial derivative of the aerodynamic parameters to the Mach number and the lift-to-drag ratio should be known. However, such parameters are generally unavailable for a noncooperative vehicle. Moreover,

considering the typical characteristics of a hypersonic gliding vehicle, the prior information about the configuration can be inferred. In this section, a parameterized model of the hypersonic technology vehicle 2 (HTV-2) is established. Then, the typical configurations are investigated to obtain the aerodynamic characteristics. Finally, the statistical analysis of the aerodynamic characteristics is performed to approximate the unknown partial derivative of the aerodynamic parameters to Mach number and the lift-to-drag ratio in nonlinear Markov maneuver accelerations.

A. PARAMETRIC MODEL OF HTV-2-LIKE HGVs

It should be indicated that although the configuration of the noncooperative HGV cannot be obtained by the defending system, its configuration is subjected to some constraints in order to achieve specific tasks. Therefore, according to the prior knowledge of the HGV, it is possible to parameterize the typical HGV approximately to provide deep insight into aerodynamic characteristics. Fig. 2 shows that HTV-2 liked configuration, which has an appropriate tradeoff in aspects of high lift drag ration and thermal protection is considered as a baseline in the present study.

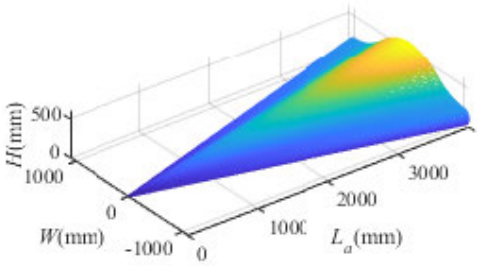

FIGURE 2. Parametric three-dimensional model of the HTV-2 HGV aerodynamic configuration.

TABLE 1. Configuration control parameters of HTV-2 HGV.

Parameters	Baseline	Maximum	Minimum	Remarks
L_a(mm)	3600	4000	3200	Maximum axial length
W(mm)	1800	2200	1400	Maximum width
s(mm)	60	100	20	Improving thermal environment
H(mm)		600		Maximum altitude
position of Bn		Bx=500, By=300		Adjust leeward surface

The configurations of the HGV similar to HTV-2 are mainly determined by the following design parameters: The full length, the height and the maximum width of the aircraft, the radius of the bottom arc and the coordinates of the shape control points in the bottom cross-section [24], [25]. Table 1 presents the contour parameters corresponding to the parametric modeling of the HGV. Moreover, Fig. 3 and Fig. 4 show the bottom cross-sections of the HGV obtained by

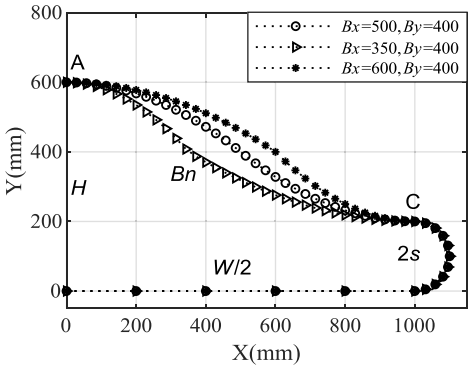

FIGURE 3. The bottom cross sections of HTV-2 (different Bn positions).

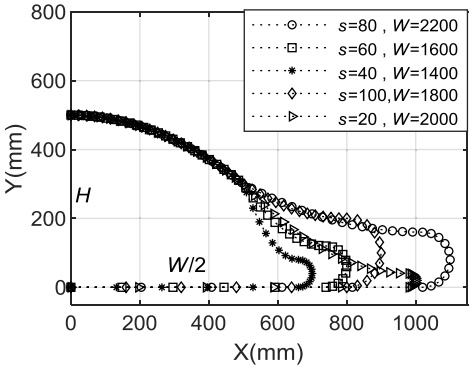

FIGURE 4. The bottom cross sections of HTV-2 (different s and W).

choosing different design parameters. It is worth noting that X and Y coincide with the axis of the aircraft body coordinate frame.

TABLE 2. Typical topological configuration parameters of HTV-2 HGV.

Configuration Control Parameters	Maximum Axial length L_a(mm)	Maximum width W(mm)	Bottom arc radius s(mm)
Model1	3400	2200	80
Model2	3200	1600	60
Model3	3800	1400	40
Model4	4000	1800	100
Model5	3600	2000	20

B. ANALYSIS OF THE AERODYNAMIC PERFORMANCE FOR THE TYPICAL CONFIGURATIONS

Table 2 shows that it is necessary to analyze the general aerodynamic performance for a family of the HGV configurations, which are generated by the optimal Latin hypercube design method [26]. Analogously, the aerodynamic characteristics of the parametric model set of HGVs are analyzed. For each configuration, the aerodynamic coefficients of the HGV are fully calculated under various flight conditions. The angle of attack varies from $-10°$ to $10°$, Mach number from 3 to 20, and altitude from 30km to 50km. For the space limitation, only the cases of Ma $= 10$ and $\alpha = 10°$ are listed as follows.

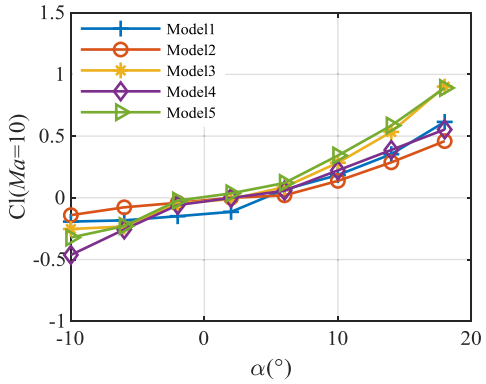

FIGURE 5. Variable trend of lift coefficient with different angles of attack.

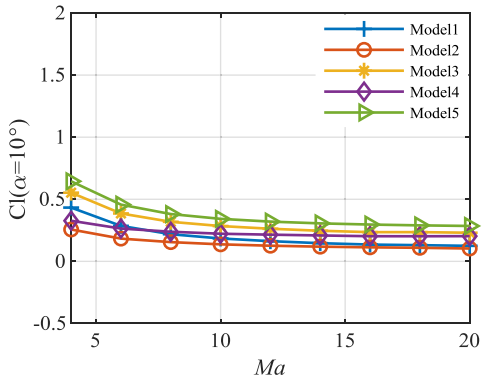

FIGURE 6. Variable trend of lift coefficient with different Mach number.

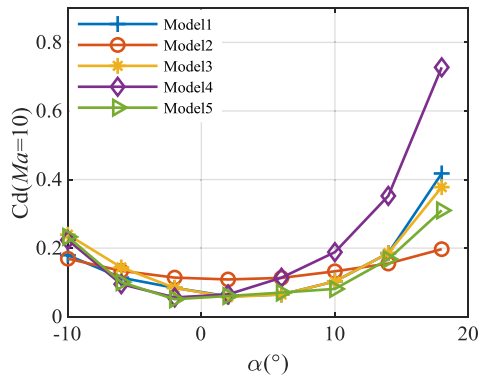

FIGURE 7. Variable trend of drag coefficient with different angles of attack.

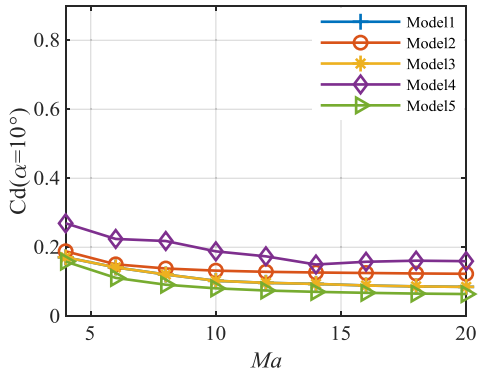

FIGURE 8. Variable trend of drag coefficient with different Mach number.

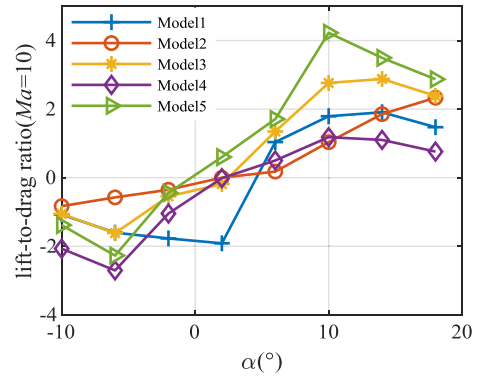

FIGURE 9. Variable trend of lift-to-drag ratio with different angles of attack.

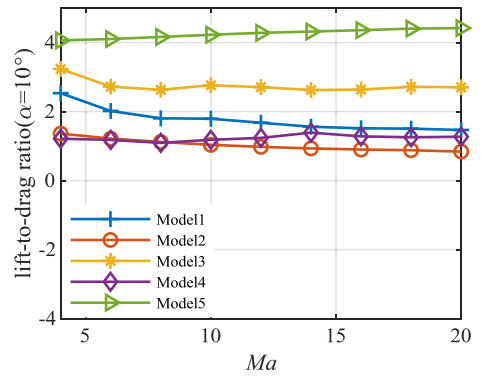

FIGURE 10. Variable trend of lift-to-drag ratio with different Mach number.

Fig. 5 to Fig. 10 show the lift coefficient, drag coefficient and lift-drag ratio with the angle of attack and Mach number at the altitude of 40 km.

The configurations in Table 2 show that (1) the lift coefficient of HGVs changes linearly with the angle of attack approximately; (2) the drag coefficient of HGVs is quadratic with the angle of attack approximately; (3) When the angle of attack remains constant, the lift coefficients and drag coefficients change almost linearly ($Ma>5$); (4) the lift coefficients and drag coefficients of HGVs negatively correlate with the Mach number; (5) the slope and intercept of the linear function of the aerodynamic coefficients concerning the Mach number are close. Therefore, the mean value of the slope and intercept can be used as the approximation of uncertain parameters.

Fig. 9 and Fig. 10 show that by studying the lift-to-drag ratio of the typical configurations, the following conclusions are drawn: (1) The maximum lift-to-drag ratio appears at about 10 degrees of the angle of attack. (2) The maximum lift-to-drag ratio of the HTV-2-like HGV is around 4, which is in accordance with the results of the existing literature [27]. (3) In general, the lift-drag ratio of the HGV positively

correlates with the angle of attack. (4) The lift-to-drag ratios of HGV are basically independent of the Mach number.

C. AERODYNAMIC PARAMETER STATISTICS

The Kernel density estimation (KDE) technique [28] is utilized to determine the probability density function (PDF) quantitatively for each unknown parameter in the acceleration component. Each PDF is expressed in $\rho_e(x)$. The mean value of the parameters, the variance and the root means square error are expressed as μ_x, P_x and S_x, respectively. These statistics are determined by numerical integrations of $\rho_e(x)$ for each parameter component:

$$\begin{aligned} \mu_x &= \int_{-\infty}^{\infty} x\rho_e(x)\,dx \\ P_x &= \int_{-\infty}^{\infty} (x-\mu_x)^2\,\rho_e(x)dx \\ S_x &= P_x + \mu_x^2 \end{aligned} \tag{25}$$

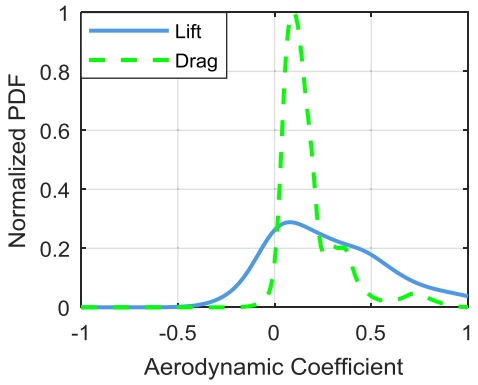

FIGURE 11. Kernel density functions for lift and drag coefficient, determined for a family of 5 configurations.

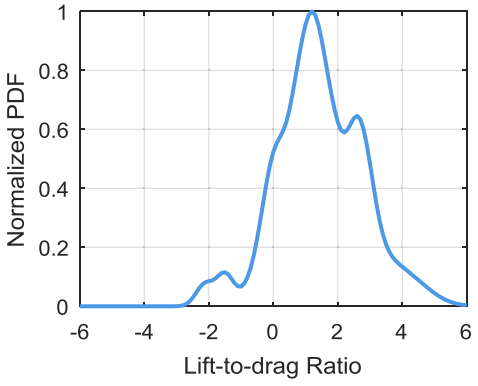

FIGURE 12. Kernel density functions for lift-to-drag ratio, determined for a family of 5 configurations.

The five configurations and flight state sets that are composed of different angles of attack and Mach numbers, define $\rho_e(x)$ for each unknown parameter components. Assuming that the flight states of the HGV are uniformly distributed, the statistical results of the probability density function at different angles of attack and Mach number are given in Fig. 11 and Fig. 12. It should be indicated that the aerodynamic coefficient and lift-drag ratio are asymmetrically distributed. For the lift coefficient, ρ_e(Cl) is distributed between -0.5 and 1, and the maximum value of the PDF appears at 0.09. For the drag coefficient, ρ_e(Cd) is distributed between 0 and 1 (even though drag is always negative), and the maximum value appears at 0.12. For the lift-to-drag ratio, $\rho_e(n)$ is distributed between -3 and 6. Table 3 gives the statistical results of aerodynamic characteristic parameters. Since the distribution of the drag coefficient is more concentrated near the maximum value, the variance and root mean square error of the drag coefficient are lower than lift coefficient.

TABLE 3. Aerodynamic characteristic parameter statistics for expected flight states.

Parameter	Lift coefficient	Drag coefficient	Lift-to-drag ratio
Mean	0.1119	0.1699	0.3927
Standard deviation	0.3437	0.1359	1.7701
Variance	0.1181	0.0185	3.1332
Root-mean-square error	0.1307	0.0473	3.2874

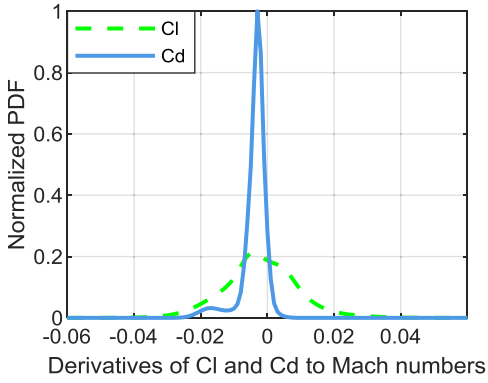

FIGURE 13. Kernel density functions for derivatives of aerodynamic coefficients to Mach numbers.

Moreover, Fig. 13 shows that the statistics of derivatives of aerodynamic coefficients to Mach numbers are also required. It is observed that the derivatives of the lift coefficient and drag coefficient to the Mach number are both negative (near zero), while the distribution of derivatives of the drag coefficients to Mach numbers is more concentrated.

TABLE 4. Derivative statistics of aerodynamic coefficient to mach number.

Parameter	Lift coefficient	Drag coefficient
Mean	-0.0020	-0.0039
Standard deviation	0.0083	0.0036
Variance	6.91×10^{-5}	1.32×10^{-5}

In summary, Table 4 presents the uncertain parameters such as derivatives of aerodynamic coefficients to Mach numbers. Moreover, the lift-to-drag ratio in Eqs. (19) and (24) are obtained by statistical methods.

What needs to be emphasized here is that the purpose of this paper is to study a novel model, which can effectively

realize the trajectory tracking for the unpowered long-range HGVs. In order to have the ability to complete some specific tasks, the aerodynamic configuration of this kind of vehicles is restricted by many constraints, such as large lift-to-drag ratio, appropriate volume ratio, etc. Therefore, the methods of parametric modelling and aerodynamic statistics proposed in this paper show the applicability in solving the tracking problem of the specific HGVs like HTV-2.

V. ITERATIVE EXTENDED KALMAN FILTER

Since the dynamics of acceleration components are established, the accelerations can be estimated by a filter. The acceleration components are augmented in the state variables. Then, the IEKF method is utilized to estimate the states of the trajectory.

A. STATE VECTOR DIFFERENTIAL EQUATION

The IEKF with nine state variables is used to estimate the 9×1 state vector and 9×9 covariance.

$$\boldsymbol{X} = \begin{bmatrix} x & y & z & v_x & v_y & v_z & a_{\mathrm{d}} & a_{\mathrm{t}} & a_{\mathrm{c}} \end{bmatrix}^{\mathrm{T}} \tag{26}$$

The elements in the state vector $\boldsymbol{X}$ include the HGV's position components x, y, z and the velocity components v_x, v_y, v_z described in the RRCS. Moreover, the acceleration components $a_{\mathrm{d}}, a_{\mathrm{t}}$ and a_{c} are resolved in the VTC coordinate frame.

The aerodynamic acceleration vector is conversed to the RRCS coordinate system, which is mathematically expressed as the following:

$$\begin{bmatrix} A_x \\ A_y \\ A_z \end{bmatrix} = T_{VTC}^{RRCS}(v) \begin{bmatrix} -a_{\mathrm{d}} \\ a_{\mathrm{t}} \\ a_{\mathrm{c}} \end{bmatrix} \tag{27}$$

where T_{VTC}^{RRCS} is the coordinate transformation matrix from the VTC coordinate frame to RRCS coordinate frame of the radar station. T_{VTC}^{RRCS} is described in terms of v [21]:

$$T_{VTC}^{RRCS}(v) = \begin{bmatrix} \frac{\dot{x}}{v} & -\frac{\dot{y}}{v_g} & -\frac{\dot{x}\dot{z}}{vv_g} \\ \frac{\dot{y}}{v} & \frac{\dot{x}}{v_g} & -\frac{\dot{y}\dot{z}}{vv_g} \\ \frac{\dot{z}}{v} & 0 & \frac{v_g}{v} \end{bmatrix} \tag{28}$$

where $v = \sqrt{\dot{x}^2 + \dot{y}^2 + \dot{z}^2}$ and $v_g = \sqrt{\dot{x}^2 + \dot{y}^2}$ are the 'total velocity' and 'in-plane velocity', respectively.

The continuous state equation of the estimation model is described as:

$$\dot{\boldsymbol{X}} = \boldsymbol{f}(\boldsymbol{X}) + \boldsymbol{w} \tag{29}$$

where $\boldsymbol{w}$ is a process noise, which is assumed to be the zero-mean Gauss white noise. The nonlinear function $\boldsymbol{f}(\boldsymbol{X})$ based on equations (19) and (24) can be expressed as:

$$\begin{cases} \dot{x} = v_x, \dot{y} = v_y, \dot{z} = v_z \\ \dot{v}_x = -\dfrac{\mu}{r^3}x + \omega^2 x + 2\omega v_y \sin B \\ \quad - 2\omega v_z \cos B + A_x \\ \dot{v}_y = -\dfrac{\mu}{r^3}y + \omega^2 y \sin^2 B - 2\omega v_x \sin B \\ \quad - \omega^2 (z + R_e) \sin B \cos B + A_y \\ \dot{v}_z = -\dfrac{\mu}{r^3}(z + R_e) - \omega^2 y \sin B \cos B \\ \quad + \omega^2 (z + R_e) \cos^2 B + 2\omega v_x \cos B + A_z \end{cases} \tag{30}$$

$$\begin{cases} \dot{a}_{\mathrm{d}} = \left(\dfrac{2}{v}\dfrac{\boldsymbol{v}^T\boldsymbol{g}}{v} - \dfrac{\partial \kappa_{\mathrm{d}}}{\partial Ma}\dfrac{1}{c_s}q - \dfrac{1}{n}\dfrac{\partial \kappa_L}{\partial Ma}\dfrac{1}{c_s}q - \dfrac{1}{hs}\dfrac{\boldsymbol{v}^T\boldsymbol{r}}{r} \right) a_{\mathrm{d}} \\ \quad - \dfrac{2}{v}a_{\mathrm{d}}^2 - \dfrac{1}{n}\dfrac{1}{\tau_L}a_L + \dfrac{\partial \kappa_{\mathrm{d}}}{\partial Ma}\dfrac{1}{c_s}\dfrac{\boldsymbol{v}^T\boldsymbol{g}}{v}q \\ \quad + \dfrac{1}{n}\dfrac{\partial \kappa_L}{\partial Ma}\dfrac{1}{c_s}\dfrac{\boldsymbol{v}^T\boldsymbol{g}}{v}q + \dfrac{1}{n}\dfrac{1}{\tau_L}a_{Lc} \\ \dot{a}_{\mathrm{t}} = \left(\left(\dfrac{\boldsymbol{v}^T\boldsymbol{g}}{v} - a_{\mathrm{d}} \right)\dfrac{2}{v} - \dfrac{1}{hs}\dfrac{\boldsymbol{v}^T\boldsymbol{r}}{r} - \dfrac{1}{\tau_{\mathrm{t}}} \right) a_{\mathrm{t}} \\ \quad + \dfrac{\partial \kappa_{\mathrm{t}}}{\partial Ma}\dfrac{1}{c_s}q\left(\dfrac{\boldsymbol{v}^T\boldsymbol{g}}{v} - a_{\mathrm{d}} \right) + \dfrac{1}{\tau_{\mathrm{t}}}a_{\mathrm{t},ctrl} \\ \dot{a}_{\mathrm{c}} = \left(\left(\dfrac{\boldsymbol{v}^T\boldsymbol{g}}{v} - a_{\mathrm{d}} \right)\dfrac{2}{v} - \dfrac{1}{hs}\dfrac{\boldsymbol{v}^T\boldsymbol{r}}{r} - \dfrac{1}{\tau_{\mathrm{c}}} \right) a_{\mathrm{c}} \\ \quad + \dfrac{\partial \kappa_{\mathrm{c}}}{\partial Ma}\dfrac{1}{c_s}q\left(\dfrac{\boldsymbol{v}^T\boldsymbol{g}}{v} - a_{\mathrm{d}} \right) + \dfrac{1}{\tau_{\mathrm{c}}}a_{\mathrm{c},ctrl} \end{cases} \tag{31}$$

By discretizing the nonlinear function $\boldsymbol{f}(\boldsymbol{X})$, the following results are obtained:

$$\boldsymbol{X}_{k+1} = \boldsymbol{X}_k + \boldsymbol{f}(\boldsymbol{X}_k, t_k)\Delta t + \frac{1}{2}\boldsymbol{F}(\boldsymbol{X}_k)\boldsymbol{f}(\boldsymbol{X}_k, t_k)(\Delta t)^2 \tag{32}$$

where, Δt is the sampling interval, which is correlated to the tracking data rate of the radar. Moreover, $\boldsymbol{F}(\boldsymbol{X}_{\mathbf{k}})$ is the Jacobian matrix of $\boldsymbol{f}(\boldsymbol{X}_{\mathbf{k}}, t_k)$, which is relative to $\boldsymbol{X}_{\mathbf{k}}$.

B. RADAR MEASUREMENT MODEL

The states of the HGVs are estimated in a mixed coordinate system. In other words, the position and velocity of the HGVs are described in the ENU rectangular coordinate system, and the measurement equation is established in the radar spherical coordinate system.

Considering the gliding trajectory of the HGV, a radar-based measurement model is proposed in the present study. The radar is assumed to measure the relative range and two gimbal angles.

$$\boldsymbol{Z}_r = \begin{bmatrix} R & A & E \end{bmatrix}^{\mathrm{T}} \tag{33}$$

where, R, A and E denote the relative range, the azimuth angle and the elevation angle, respectively.

Consequently, the nonlinear measurement equation is as follows:

$$\boldsymbol{Z}_r = \begin{bmatrix} R \\ A \\ E \end{bmatrix} = \boldsymbol{h}(\boldsymbol{x_n}) + \boldsymbol{v_n} = \begin{bmatrix} \sqrt{x^2+y^2+z^2} \\ \begin{cases} \arctan\left(x/y\right), x > 0 \\ \arctan\left(x/y\right) + \pi, x < 0, y > 0 \\ \arctan\left(x/y\right) - \pi, x < 0, y < 0 \end{cases} \\ \arctan\left(z\Big/\sqrt{x^2+y^2}\right) \end{bmatrix} + \begin{bmatrix} n_R \\ n_A \\ n_E \end{bmatrix} \tag{34}$$

where $\boldsymbol{x}_n$ represents the state in Eq (26). Moreover, n_R, n_A and n_E are radar measurement noises, assuming that they are the zero-mean white noise.

Partial derivatives of $\boldsymbol{h}(\boldsymbol{x}_n)$ with respect to the state variables specify the 3×9 measurement Jacobi matrix:

$$\boldsymbol{H}(\boldsymbol{x_n}) = \frac{\partial \boldsymbol{h}(\boldsymbol{x_n})}{\partial \boldsymbol{x_n^T}} \tag{35}$$

Measurement errors are approximated by the Gaussian random variable $\boldsymbol{v}_n$ with 3×3 variance matrix, which is described as the following:

$$\boldsymbol{R}_n = E\left\{\boldsymbol{v_n}\boldsymbol{v_n^T}\right\} \tag{36}$$

C. ITERATIVE EXTENDED KALMAN FILTER UPDATES AND PREDICTIONS

For the conventional EKF method, the Taylor expansion high-order items of $\boldsymbol{h}(\boldsymbol{x}_n)$ are omitted in the process of linearizing the observation equation [18]. During each iteration step, error will be magnified once, which leads to the worse effect of the maneuvering target state estimation or the divergence of filtering.

Moreover, the IEKF requires the algorithm to linearize the observation equation at each observation time and repeat the filtering stage to obtain the optimal estimation. The specific steps are as follows:

1) In the k-time, according to the observed data $\boldsymbol{Z}_k$, the EKF method is used to obtain the state prediction $\hat{\boldsymbol{X}}_{k/k-1}$ and the prediction covariance matrix $\boldsymbol{P}_{k/k-1}$.

2) Select the relative error between the state estimation and the observation as the variable. Eqs. (37) shows that this error is also known as the residual. Then, set a reasonable threshold according to the tolerable relative positioning error. In the iteration cycle of each step, the iteration operation is stopped when the parameter is less than the threshold value. It should be indicated that the number of iterations is expressed as N. Each initial iteration is determined by a prior estimation of the state and covariance of the previous prediction, i.e. $\hat{\boldsymbol{X}}_{k/k}^1 = \hat{\boldsymbol{X}}_{k/k-1}$ and $\boldsymbol{P}_k^1 = \boldsymbol{P}_{k/k-1}$. The filtering gain $\boldsymbol{K}_k^N$, state update $\hat{\boldsymbol{X}}_{k/k}^N$ and filtering error covariance matrix $\boldsymbol{P}_k^N$ are obtained by using the observation data at k time and the EKF updating method.

3) Let $\boldsymbol{X}_{k/k} = \hat{\boldsymbol{X}}_{k/k}^N$, $\boldsymbol{P}_k = \boldsymbol{P}_k^N$,and then use the EKF method to predict the updates by introducing the observation data at $k+1$ time. Then, repeat step 2 until the end of the filtering.

From the above steps, it is observed that the IEKF method improves the correctness of the filter covariance with nonlinear measurements. The residuals are evaluated using a nonlinear measurement function:

$$\begin{aligned} \hat{\boldsymbol{X}}_{k/k} &= \hat{\boldsymbol{X}}_{k/k-1} + \boldsymbol{K}\boldsymbol{\varepsilon}_k \\ \boldsymbol{\varepsilon}_k &= \boldsymbol{Z}_k - \boldsymbol{h}\left(\hat{\boldsymbol{X}}_{k/k-1}\right) \end{aligned} \tag{37}$$

The IEKF algorithm is an approximate method for the nonlinear system. Its iteration process is equivalent to applying the Gauss-Newton method to the iterative optimization of the least-squares residual problem.

VI. NUMERICAL SIMULATION EXPERIMENTS

In order to verify the proposed method, a simulation is conducted to track the HGV. It is worth noting that the HGV weighs 970 kg and has a reference area of 1.02 m^2. The trajectories of HGVs are generally divided into two forms, including equilibrium glide mode and skip manoeuvre mode [29]. Considering the realistic environment of the pursuit-evasion confrontation, both flight modes are tested.

It is assumed that the ground-based radar is located in the east longitude 165° and north latitude 12°. Moreover, the range of azimuth, the range of elevation and the sampling rate are $A \in [-180°, 180°)$, $E \in [0°, 20°)$ and 1 Hz, respectively. Furthermore, the standard deviation of the radial distance measurement and the standard deviation of azimuth and elevation measurements are 100 m and 2×10^{-4} rad, respectively.

For the comparison with the proposed acceleration model, three other acceleration models, including the linear Gauss-Markov processes [30], adaptive Current Statistical (CS) model [31] and the constant acceleration model [29], are utilized in the test case. The statistical average results are obtained through 100 Monte Carlo simulations. It should be indicated that root-mean-square error (RMSE) and average root-mean-square error (ARMSE) are utilized as evaluation metrics:

$$\mathrm{RMSE}_k = \sqrt{\frac{1}{M}\sum_{i=1}^{M}\left(X_k^i - \hat{X}_k^i\right)^{\mathrm{T}}\left(X_k^i - \hat{X}_k^i\right)} \tag{38}$$

$$\mathrm{ARMSE} = \frac{1}{S}\sum_{k=1}^{S}\mathrm{RMSE}_k \tag{39}$$

where, M and S denote the total number of Monte-Carlo simulations and the total steps of the simulation, respectively. Moreover, X_k^i and $\hat{X}_k^i$ are the real value and the estimation value in time $k\Delta t$ at i th simulation, respectively.

A. MODE 1: EQUILIBRIUM GLIDE MODE

In this mode, the HGV flies in the atmosphere by the equilibrium glide mode and the total acceleration in the longitudinal

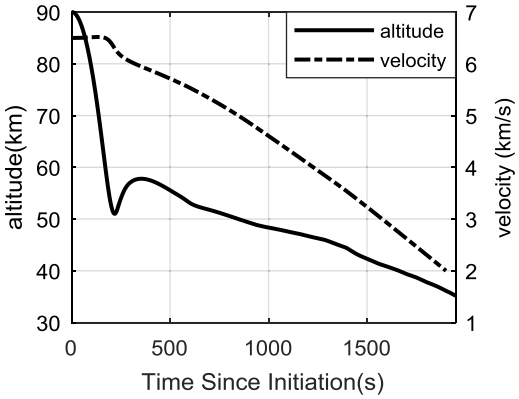

FIGURE 14. The height and velocity of HGV in the equilibrium glide mode.

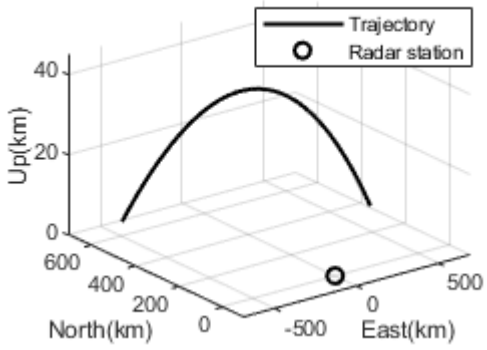

FIGURE 15. The equilibrium glide trajectory observed by the radar station.

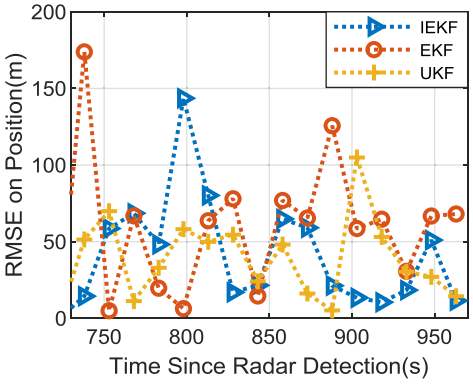

FIGURE 16. Comparison of IEKF, EKF and UKF on position estimation for equilibrium glide trajectory applying the proposed model.

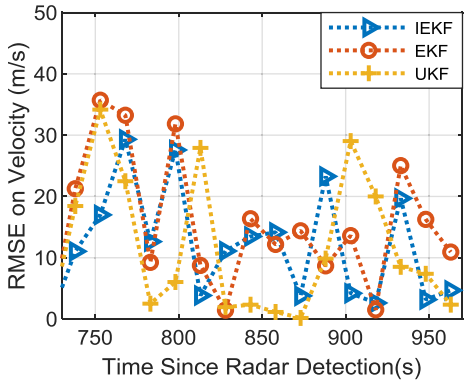

FIGURE 17. Comparison of IEKF, EKF and UKF on velocity estimation for equilibrium glide trajectory applying the proposed model.

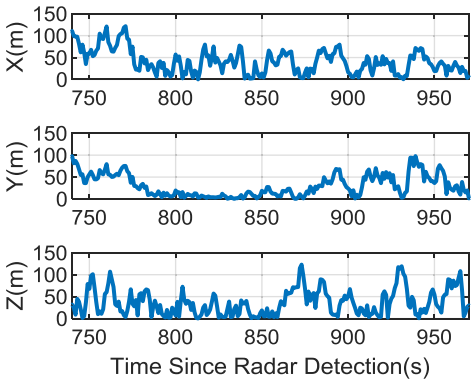

FIGURE 18. RMSEs on position estimation in X, Y and Z directions for equilibrium glide trajectory applying the proposed model.

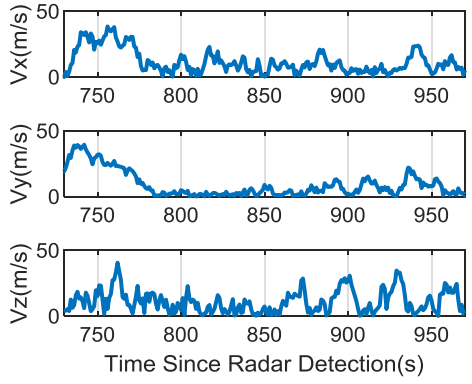

FIGURE 19. RMSEs on velocity estimation in X, Y and Z directions for equilibrium glide trajectory applying the proposed model.

plane approaches zero. The trajectory of the equilibrium gliding HGV is designed in the VTC coordinate frame from the angle of attack and bank as two control variables, which is discussed in section II. The initial altitude, velocity and path angle are 90 km, 6500 m/s and 0°, respectively. Fig. 14 shows the height and velocity distributions of the HGV during gliding. In this mode, the path angle of the HGV is small and its rate approaches zero. Fig. 15 depicts the geometric relationship between the radar and the target trajectory. The range of the equilibrium glide HGV detected by radar is more than 1200 km.

By applying the proposed model, the comparisons of EKF, UKF and IEKF on the position and velocity estimation for equilibrium glide trajectory are shown in Fig. 16 and Fig. 17. The simulation results are extracted at 15 seconds interval. Therefore, the details of the lines and points in the diagram can be clearly presented.

For the equilibrium glide scenario, Table 5 shows the ARMSEs and the runtime completed 100 Monte Carlo simulations of the three algorithms. It depicts that the average

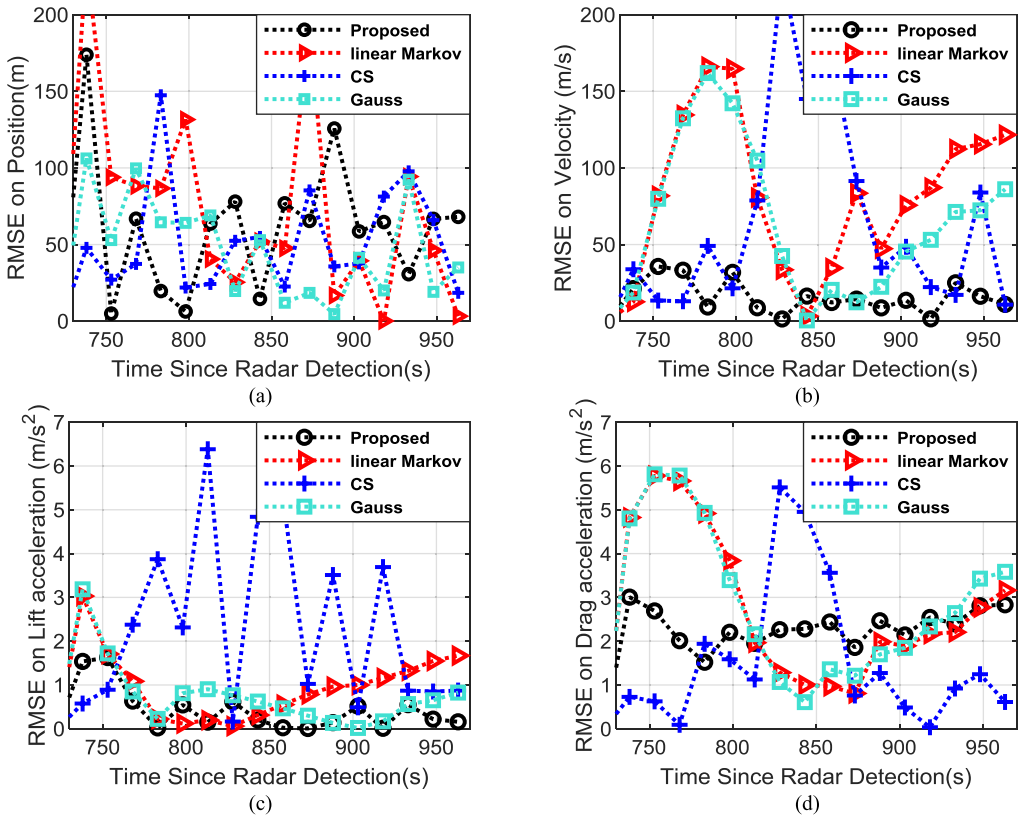

FIGURE 20. The State estimation results of equilibrium glide mode (a) Comparison of RMSEs on position estimation, (b) Comparison of RMSEs on velocity estimation, (c) Comparison of RMSEs on total lift acceleration estimation, (d) Comparison of RMSEs on drag acceleration estimation.

TABLE 5. Comparison of ARMSE and runtime of various algorithms.

Algorithms	ARMSE		Runtime (s)
	Position (m)	Velocity (m/s)	
IEKF	46.27	16.62	12.71
EKF	51.52	24.83	11.75
UKF	43.96	14.99	26.46

tracking precision of the IEKF algorithm is similar to that of the UKF algorithm, which is better than the conventional EKF algorithm. ARMSEs on position and velocity of the IEKF algorithm decrease by 10% and 33%, respectively, compared with the EKF algorithm. Although the tracking accuracy of the IEKF algorithm is slightly lower than that of the UKF algorithm, the runtime is reduced by 52%. In summary, the IEKF algorithm exhibits satisfactory accuracy and real-time performance.

For the equilibrium glide trajectory, the RMSEs on position and velocity estimation in the X, Y and Z-axis applying the proposed model are shown in Fig. 18 and Fig. 19, respectively. These results evident that the proposed model and IEKF algorithm exhibit stable tracking performance for equilibrium glide targets.

Fig. 20 shows RMSEs of the estimations on the position, velocity, lift acceleration and drag acceleration for the four filter models, respectively. Fig. 20(a) shows that there is no significant difference in the accuracy of the position estimation for these four estimation models when HGV is in the equilibrium glide mode (during 700 s to 950 s). This phenomenon is reasonable since the position of the HGV can be measured directly. The RMSE of the position estimation by the proposed model can converge to about 50 m. Moreover, Fig. 20 (b) illustrates that the velocity estimation error of the proposed acceleration model is significantly lower than that of the other three models. Since the velocity cannot be measured by the radar, the estimation of the velocity relies on the estimation accuracy of the accelerations. Furthermore, Fig. 20 (c) shows that the total lift acceleration by the proposed model obtains the highest accuracy. In Fig. 20 (d), the estimation of the drag acceleration of the proposed model does not show much higher accuracy. However, it steadily converges to a moderate value.

Table 6 presents that the ARMSE of the proposed model is significantly better than that of the other three models. It is found that the position estimation accuracy, velocity estimation accuracy and acceleration estimation accuracy are improved by about 7%, 50% and 20%, respectively.

B. MODE 2: SKIP GLIDE MODE

In this mode, the skip gliding trajectory of the HGV, including the initial altitude of 90 km and initial velocity of 6500 m/s is designed. Moreover, the angle of attack and bank are

TABLE 6. Comparison of ARMSE using various tracking models.

Models	ARMSE			
	Position (m)	Velocity (m/s)	Lift (m/s^2)	Drag (m/s^2)
Proposed	46.27	16.62	0.4508	2.3246
Linear Markov	66.27	82.42	0.9633	2.7460
CS	54.14	38.69	1.1204	2.2744
Gauss	55.81	68.81	0.6404	2.7066

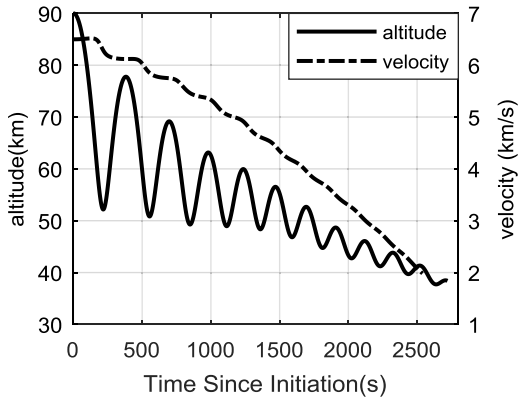

FIGURE 21. The height and velocity of HGV in the skip glide mode.

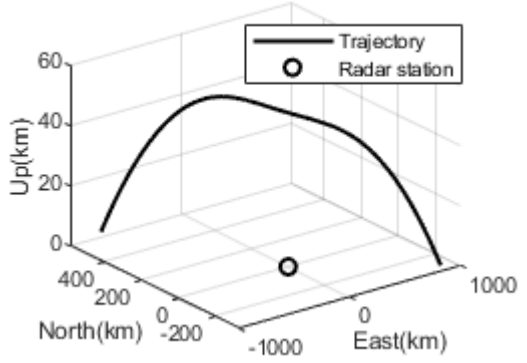

FIGURE 22. The skip glide trajectory observed by the radar station.

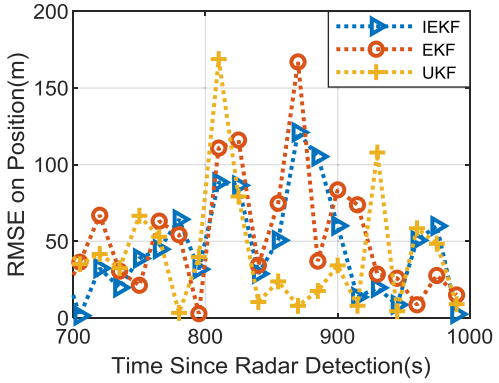

FIGURE 23. Comparison of IEKF, EKF and UKF on position estimation for skip glide trajectory applying the proposed model.

considered as two control variables. Fig. 21 shows the height and velocity of the HGV during gliding. Due to the influence of the curvature of the earth, the ground-based radar can only

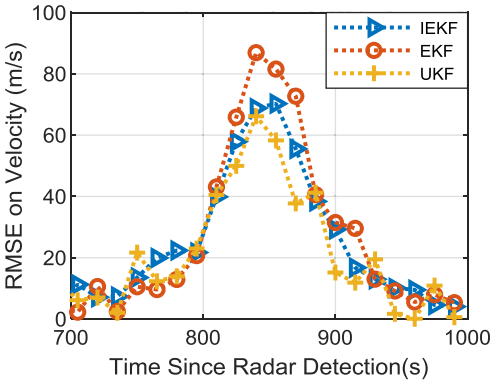

FIGURE 24. Comparison of IEKF, EKF and UKF on velocity estimation for skip glide trajectory applying the proposed model.

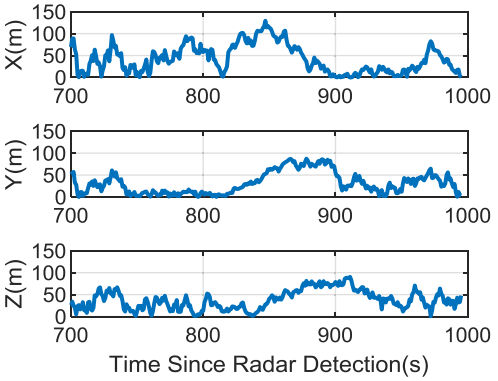

FIGURE 25. RMSEs on position estimation in X, Y and Z directions for skip glide trajectory applying the proposed model.

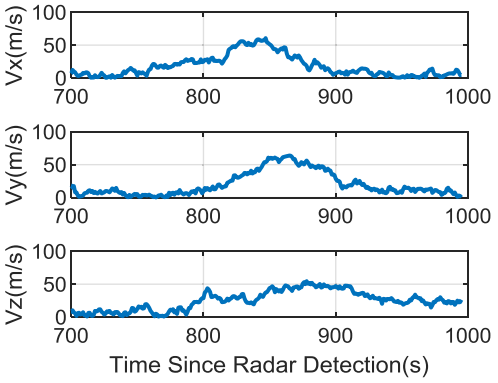

FIGURE 26. RMSEs on velocity estimation in X, Y and Z directions for skip glide trajectory applying the proposed model.

observe the HGV above the local horizon. Fig. 22 depicts the geometric relationship between the radar and the skip glide target trajectory. It is worth noting that the range of the skip glide HGV detected by radar is more than 1700 km and the observable time is about 300 s.

By applying the proposed model, the comparisons of EKF, UKF and IEKF on the position and velocity estimation for skip glide trajectory are shown in Fig. 23 and Fig. 24. The simulation results are extracted at 15 seconds interval.

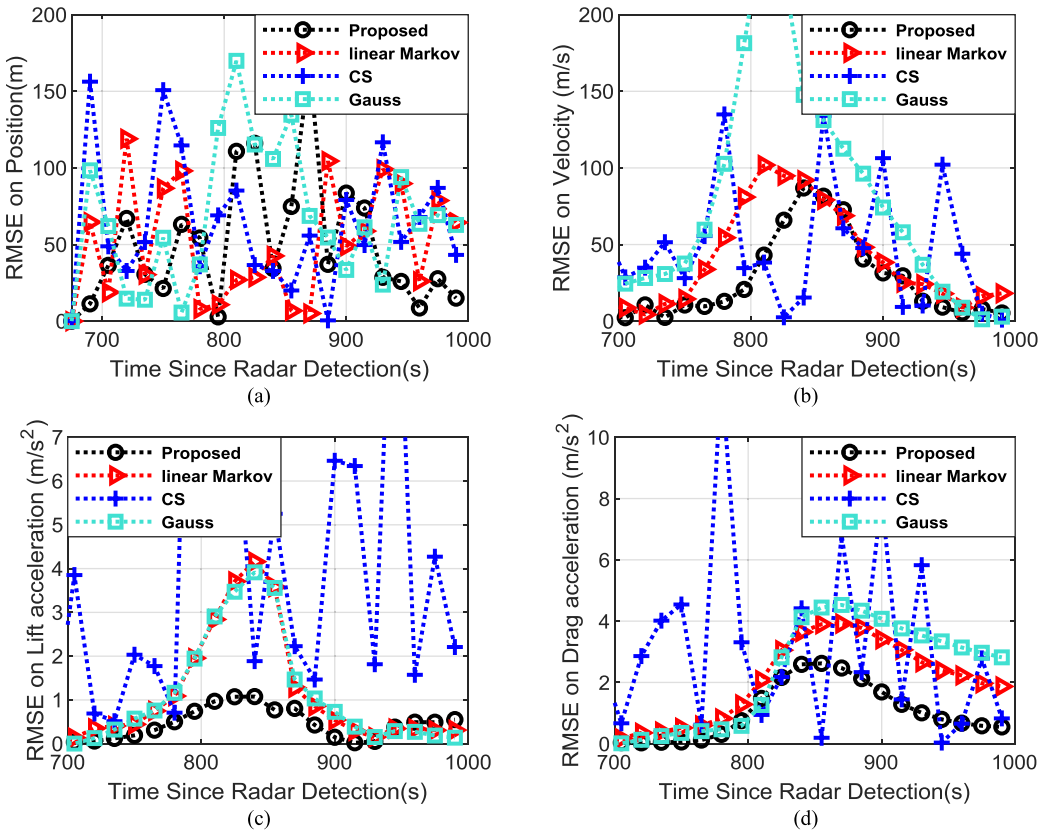

FIGURE 27. The State estimation results of skip glide mode (a) Comparison of RMSEs on position estimation, (b) Comparison of RMSEs on velocity estimation, (c) Comparison of RMSEs on total lift acceleration estimation, (d) Comparison of RMSEs on drag acceleration estimation.

For the skip glide scenario, Table 7 shows the ARMSEs and the runtime of the three algorithms. The ARMSEs on position and velocity of the IEKF algorithm decrease by 11% and 16%, respectively, compared with the EKF algorithm. Indeed, using UKF algorithm can improve the tracking accuracy of skip glide trajectory to some extent, however, the computational burden of the IEKF algorithm is much less than the UKF algorithm.

TABLE 7. Comparison of ARMSE and runtime of various algorithms.

Algorithms	ARMSE		Runtime (s)
	Position (m)	Velocity (m/s)	
IEKF	54.46	27.42	16.94
EKF	61.51	32.77	15.19
UKF	49.68	26.25	34.97

For skip glide trajectory, the RMSEs on position and velocity estimation in the X, Y and Z-axis applying the proposed model are shown in Fig. 25 and Fig. 26, respectively. Since the HGV performs skip maneuver between 800s and 900s, the RMSE of position and velocity estimation increases to about 100 m and 50m/s respectively. And then, the filter converges quickly, the proposed model achieves satisfied estimation precision.

Fig. 27 shows RMSEs on the position estimation, velocity estimation, lift acceleration estimation and drag acceleration estimation of the four models. Fig. 27 (a) and Fig. 27 (b) illustrate that the position and velocity estimation accuracy in the abovementioned four filter models is close to each other, and the proposed model shows a reasonable superiority in the estimation accuracy. Moreover, the RMSE of the position estimation by the proposed model can converge to about 30 m and the RMSE of the velocity estimation converges to about 20 m/s.

Furthermore, Fig. 27 (c) and Fig. 27 (d) show RMSEs of the acceleration estimation of the four models. It is observed that the tracking precision on the accelerations of the proposed model is more reasonable than the other three models.

TABLE 8. Comparison of ARMSE using various tracking models.

Models	ARMSE			
	Position (m)	Velocity (m/s)	Lift (m/s^2)	Drag (m/s^2)
Proposed	54.46	27.42	0.4664	0.9954
Linear Markov	55.11	40.09	1.1523	1.9534
CS	58.75	30.87	2.1316	3.7342
Gauss	72.71	76.94	1.1381	2.2006

Table 8 presents the tracking results quantitatively. It is found that the proposed model improves the position estimation accuracy, velocity estimation accuracy and

acceleration estimation accuracy by about 10%, 40% and 50%, respectively.

Consequently, the Gauss model describes the non-maneuvering motion of the target, which is significantly different from the real HGV motion. While the linear Markov model is suitable for the maneuver motion between constant velocity and constant acceleration, its estimation precision decreases greatly if the target performs a type of strong maneuver. For the CS model, although it can describe the current acceleration accurately, the limitations of the linear Markov model still exist.

VII. CONCLUSION

Motion modes of HGV are complex and uncertain. Therefore, the conventional estimation models cannot describe the HGV motion characteristics accurately. In the present study, the nonlinear characteristic of the gliding dynamics is considered. Then, differentials of the maneuvering acceleration components are modelled by analyzing the statistics of typical maneuvers and configurations. Moreover, an integrated nonlinear Markov acceleration model is formulated to match the nonlinear dynamics of the HGV. In order to obtain the primary information of the aerodynamic characteristics of the HGV, a class of HGV configurations is analyzed and a statistical model for the aerodynamic characteristics is established. Finally, IEKF is used to estimate the trajectory with the proposed model. The simulations for two maneuver modes of HGV are performed. It is concluded that the proposed model is able to improve the trajectory estimation accuracy effectively.

REFERENCES

[1] L. He and X. Yan, "Adaptive terminal guidance law for spiral-diving maneuver based on virtual sliding targets," *J. Guid., Control, Dyn.*, vol. 41, no. 7, pp. 1591–1601, Jul. 2018.

[2] C. Li, H. Dong, J. Li, and F. Wang, "Distributed Kalman filtering for sensor network with balanced topology," *Syst. Control Lett.*, vol. 131, Sep. 2019, Art. no. 104500.

[3] S. Li, H. Lei, L. Shao, and C. Xiao, "Multiple model tracking for hypersonic gliding vehicles with aerodynamic modeling and analysis," *IEEE Access*, vol. 7, pp. 28011–28018, 2019.

[4] Z. Duan and X. R. Li, "Modeling of target motion constrained on straight line," *IEEE Trans. Aerosp. Electron. Syst.*, vol. 52, no. 2, pp. 548–562, Apr. 2016.

[5] K. Yang, Y. Bar-Shalom, P. Willett, R. Ben-Dov, and B. Milgrom, "Observability of a thrusting/ballistic trajectory in 3-D from a single fixed passive sensor," *IEEE Trans. Aerosp. Electron. Syst.*, vol. 54, no. 6, pp. 2971–2979, Dec. 2018.

[6] F. Li, J. Xiong, Z. Qu, and X. Lan, "A damped oscillation model for tracking near space hypersonic gliding targets," *IEEE Trans. Aerosp. Electron. Syst.*, vol. 55, no. 6, pp. 2871–2890, Dec. 2019.

[7] R. Singer, "Estimating optimal tracking filter performance for manned maneuvering targets," *IEEE Trans. Aerosp. Electron. Syst.*, vol. AES-6, no. 4, pp. 473–483, Jul. 1970.

[8] B. Ozkaya and C. C. Arcasoy, "Analytical solution of discrete colored noise ECA tracking filter," *IEEE Trans. Aerosp. Electron. Syst.*, vol. 34, no. 1, pp. 93–102, Jan. 1998.

[9] I. Klein, Y. Bar-Shalom, and I. Rusnak, "Observability analysis for tracking of coordinated turn maneuvers," in *Proc. IEEE 28th Conv. Electr. Electron. Engineers Isr. (IEEEI)*, Dec. 2014, pp. 1–5.

[10] R. Moose, "An adaptive estimator with learning for a plant containing semi-Markov switching parameters," *IEEE Trans. Syst., Man, Cybern.*, vol. SMC-3, no. 3, pp. 277–281, May 1973.

[11] K. Mehrotra and P. R. Mahapatra, "A jerk model for tracking highly maneuvering targets," *IEEE Trans. Aerosp. Electron. Syst.*, vol. 33, no. 4, pp. 1094–1105, Oct. 1997.

[12] H. Zhang, J. Xie, J. Ge, W. Lu, and B. Liu, "Strong tracking SCKF based on adaptive CS model for manoeuvring aircraft tracking," *IET Radar, Sonar Navigat.*, vol. 12, no. 7, pp. 742–749, Jul. 2018.

[13] P. N. Dwivedi, P. G. Bhale, A. Bhattacharyya, and R. Padhi, "Generalized state estimation and model predictive guidance for spiraling and ballistic targets," *J. Guid., Control, Dyn.*, vol. 37, no. 1, pp. 243–264, Jan. 2014.

[14] C.-B. Chang, M. Athans, and R. Whiting, "On the state and parameter estimation for maneuvering reentry vehicles," *IEEE Trans. Autom. Control*, vol. AC-22, no. 1, pp. 99–105, Feb. 1977.

[15] Y. Fan, W. Zhu, and G. Bai, "A cost-effective tracking algorithm for hypersonic glide vehicle maneuver based on modified aerodynamic model," *Appl. Sci.*, vol. 6, no. 10, p. 312, Oct. 2016.

[16] O. B. Dubois-Matra and Robert, "Tracking and identification of a maneuvering reentry vehicle," presented at the AIAA Guid., Navigat., Control Conf. Exhibit, Austin, TX, USA, 2003.

[17] R. H. Bishop, "Bayesian estimation for tracking of spiraling reentry vehicles," in *Proc. AIAA Guid., Navigat., Control (GNC) Conf.*, Aug. 2013, p. 5126.

[18] M. E. Hough, "Reentry maneuver estimation using nonlinear Markov acceleration models," *J. Guid., Control, Dyn.*, vol. 40, no. 7, pp. 1693–1710, Jul. 2017.

[19] X. Yan and L. He, "Unpowered approach and landing trajectory planning using second-order cone programming," *Aerosp. Sci. Technol.*, vol. 101, Jun. 2020, Art. no. 105841.

[20] G. Li, H. Zhang, and G. Tang, "Maneuver characteristics analysis for hypersonic glide vehicles," *Aerosp. Sci. Technol.*, vol. 43, pp. 321–328, Jun. 2015.

[21] X. R. Li and V. P. Jilkov, "Survey of maneuvering target tracking. Part II: Motion models of ballistic and space targets," *IEEE Trans. Aerosp. Electron. Syst.*, vol. 46, no. 1, pp. 96–119, Jan. 2010.

[22] N. X. Vinh, *Optimal Trajectories in Atmospheric Flight*. Amsterdam, The Netherlands: Pergamon, 1982, pp. 73–81.

[23] F. J. Regan and S. M. Anandakrishnan, *Dynamics of Atmospheric Re-Entry*. Reston, VA, USA: American Institute Aeronautics Astronautics, 1993, pp. 179–207.

[24] J. A. Samareh, "Survey of shape parameterization techniques for high-fidelity multidisciplinary shape optimization," *AIAA J.*, vol. 39, pp. 877–884, Jan. 2001.

[25] B. M. Kulfan, "Universal parametric geometry representation method," *J. Aircr.*, vol. 45, no. 1, pp. 142–158, Jan. 2008.

[26] J. C. Helton and F. J. Davis, "Latin hypercube sampling and the propagation of uncertainty in analyses of complex systems," *Rel. Eng. Syst. Saf.*, vol. 81, no. 1, pp. 23–69, Jul. 2003.

[27] S. Walker, J. Sherk, D. Shell, R. Schena, J. Bergmann, and J. Gladbach, "The DARPA/AF falcon program: The hypersonic technology vehicle #2 (HTV-2) flight demonstration phase," in *Proc. 15th AIAA Int. Space Planes Hypersonic Syst. Technol. Conf.*, Apr. 2008, p. 2339.

[28] B. Silverman, *Density Estimation for Statistics and Data Analysis*. London, U.K.: Chapman & Hall, 1986, pp. 75–93.

[29] J. Zhu, R. He, G. Tang, and W. Bao, "Pendulum maneuvering strategy for hypersonic glide vehicles," *Aerosp. Sci. Technol.*, vol. 78, pp. 62–70, Jul. 2018.

[30] Q. Lei, L. Junlong, and Z. Di, "Tracking filter and prediction for non-ballistic target HTV-2 in near space," in *Proc. 27th Chin. Control Decis. Conf. (CCDC)*, May 2015, pp. 3556–3561.

[31] H. Zhang, J. Xie, J. Ge, W. Lu, and B. Zong, "Adaptive strong tracking square-root cubature Kalman filter for maneuvering aircraft tracking," *IEEE Access*, vol. 6, pp. 10052–10061, 2018.

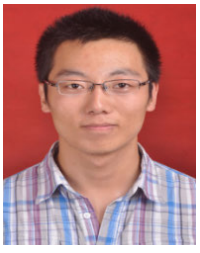

YUNPENG CHENG received the B.S. and M.S. degrees from Northwestern Polytechnical University, Xi'an, China, in 2014 and 2016, where he is currently pursuing the Ph.D. degree in flight vehicle design with the School of Astronautics. His current research interests include maneuvering target tracking and flight dynamics.

SHUO TANG received the B.S., M.S., and Ph.D. degrees from Northwestern Polytechnical University, Xi'an, China, in 1982, 1985, and 1988, respectively. He is currently a Professor with the School of Astronautics, Northwestern Polytechnical University, Xi'an. His current research interests include aerospace vehicle design, flight dynamics, flight simulation, and virtual prototype technology.

SHI LYU was born in Nanchong, Sichuan, China, in 1988. He received the B.S., M.S., and Ph.D. degrees in aerospace designing from Northwestern Polytechnical University, Xi'an, China, in 2010, 2013, and 2019, respectively.

From 2015 to 2017, he was a Visiting Ph.D. Student with the Space Engineering Design Laboratory, York University, Toronto, Canada, supported by the China Scholarship Council. He is currently an Associate Researcher with the School of Astronautics, Northwestern Polytechnical University. His research interests include guidance law design, adaptive control, and sliding mode control.

MANQIAO WU received the B.S. and M.S. degrees in aerospace science and technology from Northwestern Polytechnical University, Xi'an, China, in 2015 and 2018, respectively. Her current research interests include intelligent structure, aerospace vehicle design, guidance law design, and adaptive control.

HAO QIAO received the B.S., M.S., and Ph.D. degrees from Northwestern Polytechnical University, Xi'an, China, in 2012, 2016, and 2019, respectively. His current research interests include cooperative trajectory planning and reentry guidance.